Observational estimates of air mass with temperatures conducive to arctic polar stratospheric clouds

M. de la Torre Juárez[1] A. Dörnbrack[2], G.A. Hajj[1], B.A. Iijima[1], R. Kivi[3], A.J. Mannucci[1] T.M. Schrøder[1,4]

Short title: ESTIMATES OF AIR MASS CONDUCIVE TO PSCS

[1]Jet Propulsion Laboratory/California Institute of Technology, Pasadena, CA 91189.

[2]DLR, Institut für Physik der Atmosphäre, Oberpfaffenhofen, Germany.

[3]FMI, Arctic Research Centre, 99600 Sodankylä, Finland.

[4]National Research Council program of the National Academy of Sciences.

Abstract. We use GPS radio occultation (GPSRO) temperature profiles measured after 2001 by the CHAMP and SAC-C experiments to survey how much of the polar stratospheric air mass is subject to temperatures conducive to polar stratospheric clouds (PSCs). This observational survey is compared to estimates using the publicly available version of ECMWF. To single out the impact of temperature fluctuations captured by GPSRO, we also separate occultation profiles very similar to interpolated ECMWF profiles but differing in the small scale temperature fluctuations captured by GPSRO and absent in the lower vertical resolution of the ECMWF pressure levels. The total mass of the air column above 11 km colder than the Hanson-Mauersberger threshold for the formation of type I PSCs north of $65°$N found in the ECMWF global analyses is typically lower than in occultations. Because temperatures per se are not conclusive on the existence of PSCs, observations of PSCs by aerosol backscatter sondes launched in December 2001 at $67.4°$N, $26.6°$E are compared to nearby GPS profiles confirming that they are likely to occur together. GPSRO finds several layers of potential PSC formation most likely associated with a vertically propagating internal gravity wave. We also use GPSRO occultation to characterize stratospheric temperature fluctuations, stratospheric warmings during the polar night, and how they relate to the months with maximum air masses conducive to PSCs.

Introduction

Polar Stratospheric Clouds (PSCs) play an important role in the processes leading to ozone depletion in the polar stratosphere [*Montzka et al.*, 2003; *Rex et al.*, 2004]. Because of their role in modulating ozone concentrations, proper characterization of the thermodynamic background in which PSCs form and evolve is necessary to better understand the ozone budget and improve prediction capabilities. PSCs are composed of liquid supercooled ternary solutions (STS) [*Tabazadeh et al.*, 1994; *Carslaw et al.*, 1994, e.g.], or of solid nitric acid trihydrate (NAT) [*Hanson and Mauersberger*, 1988], or of ice particles. The formation mechanism of solid PSC particles is still a matter of debate. Recent studies [*Larsen et al.*, 2004; *Drdla and Browell*, 2004] have shown that homogeneous freezing mechanisms above the ice frost point temperature could explain observations of solid particles formed under synoptic scale conditions. An alternative pathway for NAT formation is heterogeneous nucleation on ice particles. In the Arctic polar vortex widespread NAT particle formation on ice is possible under mountain wave cooling conditions [*Carslaw et al.*, 1999; *Dörnbrack et al.*, 2001]. Only balloon-borne sondes, some airborne platforms, and LIDAR instruments can measure the temperature fluctuations in these waves at restricted times and Arctic locations such as Eureka (Canada) or Sodankylä (Finland). But the geographic coverage needed for representative estimates of air mass budgets subject to temperatures conducive to PSCs typically requires the temperature fields from weather analyses such as the one from the European Center for Medium-Range Weather Forecasts (ECMWF).

Estimates of air mass conducive to PSCs using ECMWF temperatures have been compared to estimates using radiosondes [*Knudsen*, 2003, and references therein]. Temperature biases in ECMWF confirmed in comparisons against other analyses [*Manney et al.*, 2003], and the lower vertical resolution in ECMWF ($\gtrsim 1.5$ km), were found to impact the estimates. In this work we describe and validate the use of temperature profiling with radio occultations of the Global Positioning System signals (GPSRO)

captured after October 2001 to survey how much air had temperatures conducive to PSCs. GPSRO provides atmospheric temperature profiles up to the stratosphere, much like radiosondes, and with denser coverage. We compare the air mass budgets prone to PSC formation derived from GPSRO to the semi-daily ECMWF-TOGA dataset [*DSS-UCAR*, 2004] (the pressure levels of the ECMWF analysis made widely available to the research community), interpolated to the locations of each GPSRO occultation. In the next section we discuss the characteristics of GPSRO profiles and their possible errors in the stratosphere. We compare the soundings to the ECMWF analysis and coincident radiosondes. In the second section we explain the criteria used to select the GPSRO profiles for our study. In the third section we present and discuss the results. We show first the dense coverage of GPSRO which allows for a high spatio-temporal resolution of areas which might have temperatures conducive to PSCs. We then illustrate a comparison of temperature profiles crossing the PSC threshold to in-situ backscatter soundings of actual PSCs. We finish this section by showing how the months with the most PSC temperatures correlate with large temperature wave activity and stratospheric warmings. At the end we summarize and discuss the conclusions that might be important for polar stratospheric studies.

Data

Global Positioning System radio occultations are active limb soundings in which a GPS receiver aboard a satellite tracks the GPS radio signals as they occult behind the Earth's atmosphere. The atmospheric density gradients delay and bend the radio signal. The bending angle can be inferred from the signal delay [*Fjeldbo and Eshleman*, 1965]. GPSRO bending angles are converted into radio-refractivity, N, as a function of height. N depends on total pressure, p, water vapor pressure, e,

and temperature, T, as

$$N = a_1 \frac{p}{T} + \left(a_2 + \frac{a_3}{T} \right) \frac{e}{T} \tag{1}$$

with $a_1 = 77.6$ K/hPa, $a_2 = -12.81$ K/hPa, $a_3 = 3.739 \times 10^5$ K^2/hPa [*Thayer*, 1974; *Bevis et al.*, 1994]. In the stratosphere, the water vapor contribution, e, is too small to be detected and can be ignored, so that refractivity N is proportional to atmospheric density. Refractivity profiles can thus be used to infer high vertical resolution temperature profiles as a function of height from the mid-troposphere to the stratosphere [*Kursinski et al.*, 1996] along 200-300 km long ray paths. While radiosondes in the Arctic are subject to frequent bursts at heights between 21 and 25 km [*Randel and Wu*, 1999, e.g.], GPSRO typically reach above these heights. They also seem ideally suited for polar studies because they provide dense accurate sampling over remote regions where PSCs can form.

Data error sources

Two major sources of temperature data are discussed in this work: the public version of the ECMWF analysis, and GPSRO temperature profiles.

The public version of the ECMWF analysis (or ECMWF-TOGA) has a horizontal resolution of 2.5°×2.5° in latitude and longitude. The model is run at 60 level vertical resolution but only the values corresponding to 22 pressure levels are made available. For the polar regions, a lower amount of assimilated data increases the uncertainty of the ECMWF analyses. Radiosonde, pilot balloons, or profiler data do not cover the Arctic Ocean, aircraft reports rarely reach latitudes north of 70°N or south of 60°S, and infrared or microwave radiances from polar-orbiting satellites remain difficult to use in polar regions because of poor discrimination between clouds and ice or poor representation of the surface emissivity. As a consequence, validation of the ECMWF model is difficult in these areas, and the impact of its errors on our scientific understanding of polar processes remains a subject of active

research [*de la Torre Juárez*, 2002; *Manney et al.*, 2003; *Knudsen*, 2003, e.g.].

The second dataset is temperature profiles derived from GPSRO. They typically agree with coincident radiosondes to within 1 K up to 24 km [*Kursinski et al.*, 1996; *Rocken et al.*, 1997, e.g.]. They have been also shown to capture accurately the temperature signatures of gravity waves up to 35 km [*Preusse et al.*, 2000; *Tsuda et al.*, 2000; *de la Torre et al.*, 2004]. The sources of error for GPSRO have been extensively documented [*Kursinski et al.*, 1996, 1997; *Hocke*, 1997; *Kursinski et al.*, 2000; *Hajj et al.*, 2004; *Gobiet and Kirchengast*, 2004, e.g.]. Studies of the errors particular to the two satellites used here have also been characterized [*Hajj et al.*, 2004] showing that differences between coincident GPSRO from different GPSRO receivers are below 0.2 K standard deviation (an occultation captured by a receiver aboard one spacecraft compared to another captured by the GPS receiver aboard a second satellite). The sources of error in the polar stratosphere are discussed next for our particular data set.

Above 25 km the measured occultation bending angles display high frequency variability that increases with height. This variability can cause biases in the stratospheric GPSRO temperature profiles [*Kursinski et al.*, 1997; *Hocke*, 1997; *Kursinski et al.*, 2000; *Hajj et al.*, 2004]. The details of how the Abel bending angle integral [*Fjeldbo and Eshleman*, 1965; *Hajj et al.*, 2002] is performed in this region can lead to improvements in stratospheric temperatures. Two approaches are currently most popular. The first uses a statistical optimization technique [*Gobiet and Kirchengast*, 2004, and references therein] to generate the GPSRO temperature profiles in the stratosphere. It uses a weighted average between a climatological model climatology and the GPSRO data. The weights are chosen to minimize the root mean square (RMS) difference between GPSRO bending angles and the model. The averaging gives large weights to the model at altitudes and seasons with high fluctuations and slowly transitions to occultation data at lower altitudes. This method requires reasonable estimates of

the variance and covariance characteristics of the measurements and model and they are not clearly established yet. While it provides GPSRO temperature profiles at high altitudes, such temperatures are largely influenced by the model and the height where they become fully occultation-based is variable, depending on the RMS values for the bending angles in each occultation. The second retrieval approach will be termed as the "extrapolation approach". It consists in the exponential extrapolation up to infinity of an exponential fit to the GPSRO bending angle in a height range known to have typically low bending angle RMS [*Hajj et al.*, 2002]. The extrapolation is made assuming an exponential bending angle decay with constant scale height above this region. We chose this approach because it is less likely to filter out the natural stratospheric fluctuations captured by the data and which would translate as bending angle fluctuations. While the exponential approximation is subject to the error associated with assuming an exponential bending angle decay with height, it has been validated to provide the lowest model independent temperature biases when the fit is made near the stratopause (44-55 km) [*Schrøder et al.*, 2005]. In numerical simulations comparing both approaches, the exponential approach has shown a similar (albeit smaller) temperature bias [*Ao et al.*, 2005]. The extrapolation approach has mainly two advantages. First, that the inferred atmospheric bending angles and radio-refractivities (i.e. densities in the stratosphere). are model independent; and second, that it does not artificially suppress stratospheric fluctuations.

We applied the extrapolation approach to generate GPSRO refractivity profiles with $\lesssim$1 km vertical resolution to the data captured by GPS receivers aboard the low Earth orbiting satellites CHAMP (Challenging Mini-Satellite Payload for Geophysical Research and Application) and SAC-C (Satélite de aplicaciones Científicas-C). The bending angle integral was initialized using only the data at 55 km after a fit to 10 height levels. These initialization parameters are only slightly different from the ones described in *Hajj et al.* [2004] but chosen to reduce stratospheric temperature biases.

An additional source or temperature biases in GPSRO profiles stems from the conversion from refractivities to temperatures which requires performing the hydrostatic balance integral [*Fjeldbo and Eshleman*, 1965; *Hajj et al.*, 2002, for our specific data set]. To initialize this integral the temperature from the occultation is assumed to equal that of the ECMWF-TOGA interpolated to the location of the occultation at the initialization height z_o =41 km. Assigning the model temperature to the occultation at 41 km causes an error because occultation and analysis are not exactly equal and thus refractivities differ. The nature of this error is described next. For our error analysis we use next the subscript "o" to refer to the "true" occultation profile, "r" for the one we retrieve, and "e" for the ECWMF analysis. Because occultation and model refractivities differ by $\varepsilon_N = N_e(z_o = 41km)/N_o(z_o = 41km) - 1$, forcing $T_r(z_o) = T_e(z_o)$ introduces an error in pressure in addition to the error $\varepsilon_p = p_e(z_o)/p_o(z_o) - 1$ caused by a difference in pressure versus height values between occultation and analysis. To focus only on the impact of assuming $T_e(z_o) = T_r(z_o)$, we assume that the retrieved and the true occultation refractivities agree ($N_r(z_o) = N_o(z_o)$). Ignoring the water vapor contributions, equation (1) is forced to be:

$$N_o(z_o) = N_r(z_o) = a_1 \frac{p_r(z_o)}{T_e(z_o)} = N_e(z_o) \frac{p_r(z_o)}{p_e(z_o)} =$$
$$= \frac{p_r(z_o) N_o(z_o)(1 + \varepsilon_N)}{p_o(z_o)(1 + \varepsilon_p)}$$

Using $\varepsilon_{rp} = p_r(z_o)/p_o(z_o) - 1$ for the error in our estimate of the occultation pressure implies:

$$\varepsilon_{rp} = \frac{\varepsilon_p - \varepsilon_N}{1 + \varepsilon_N} \tag{2}$$

We do not know how big ε_p is, but we ignore it for now to isolate the impact of the temperature initialization. Hence, if the analysis were the "truth" value, and a refractivity difference of 10% ($\varepsilon_N = 0.1$) were found, the retrieval initialization would have a pressure shift of -9%. At 41 km, this bias would be of the order of a 9% of 1 hPa. On the other hand, if the occultation is "truth", this

initialization introduces an erroneous pressure shift.

This pressure bias leads to an error in temperatures below z_o through the hydrostatic balance integral, but as pressure increases, the relative importance of this bias decreases as a power law [*de la Torre Juárez et al.*, 2004; *Hajj et al.*, 2004, e.g.] and so does the temperature error. The contribution by the pressure shift to the error below the initialization height (i.e. ignoring any other error sources) can be estimated by imposing the condition that $p_o(z) - p_o(z_o) = p_r(z) - p_r(z_o)$ so that the impact on the retrieved temperature can be found from:

$$N_o(z) = N_r(z) = a_1 \frac{p_r(z)}{T_r(z)} = a_1 \frac{p_o(z) + [p_r(z_o) - p_o(z_o)]}{T_r(z)}$$

which leads to the following relation between retrieved and occultation temperature:

$$T_r(z) = a_1 \left[\frac{p_o(z)}{N_o(z)} + \frac{p_r(z_o) - p_o(z_o)}{N_o(z)} \right] =$$

$$T_o(z) + \frac{N_o(z_o) T_r(z_o) \varepsilon_{rp}}{N_o(z)(1 + \varepsilon_{rp})}$$

or equivalently, using expression (2),

$$T_r(z) - T_o(z) = \frac{\varepsilon_p - \varepsilon_N}{1 + \varepsilon_p} \left[\frac{N_o(z_o)}{N_o(z)} \right] \times T_r(z_o) \tag{3}$$

The ratio of refractivities in formula (3) makes the error due to temperature initialization decay proportionally to the inverse of density. The impact of the initialization error on the $T_r(z) - T_e(z)$ difference is typically found to peak immediately below the initialization height [*de la Torre Juárez et al.*, 2004; *Hajj et al.*, 2004; *Ao et al.*, 2005]. This is also seen in our dataset on figure 1 top. In this figure the ECMWF analysis temperatures closest in time to the GPSRO were interpolated to the locations and heights of the occultation temperatures and subtracted. The differences were then averaged on a biweekly basis to 0.5 km bins. To guide the eye, vertical dashed grey lines mark the half year and the new year. Contours are plotted each 0.5 K and labeled each 1 K. The comparison was

limited to occultations which differed from the interpolated ECMWF analysis by less than 10K and 10% refractivity at all heights above 4 km. Mean differences are sub-Kelvin at most heights most of the time with the analysis being typically colder than the occultations. This cold bias of ECMWF against GPSRO agrees with results for shorter time periods in comparisons against CHAMP GPSRO [*Gobiet et al.*, 2005] and against radiosondes [*Knudsen*, 2003]. The largest differences, above 1 K, are found typically near 35 km, where a seasonal behavior is observed: each winter's occultations seem to be warmer than the analysis by more than 1 K below 30 km. The winter of 2004/2005 also shows a large cold anomaly near 40 km.

Figure 1.

Validation

As an independent validation, figure 1 bottom compares all the GPSRO north of 65°N, with "coincident" radiosondes, within 500 km and 6 hours, during April 2001–August 2002. It shows the histogram of temperature differences radiosondes minus coincident GPSRO. Differences larger or equal to $\pm$10 K were counted as $\pm$10 K. To compensate for the geographical distance, radiosonde values were extrapolated to the GPSRO location using horizontal temperature gradients from ERA-40. Pressure levels at 100 hPa (thick grey) and 70 hPa (thin black) show a peak in the -1 K–0 K range with GPSRO being warmer. At 10hPa (dots), 20hPa (dashed), and 50hPa, the peak is at 0 K–1 K with a larger spread, consistent with an increase of temperature fluctuations with height. The low number of differences in the $\geq$10K regime shows that most occultations differ little from the radiosonde temperatures.

Figure 2.

Table 1.

Two further validation comparisons are presented in figure 2. The first (left) is between radiosondes and GPSRO without using the horizontal gradients from ERA-40 to interpolate from the radiosonde location to the occultation tangent points. Without this interpolation the histogram widens. The second comparison, in figure 2 right, compares the ECMWF analysis at the location of the

occultation and exact time of the radiosonde against the radiosonde. Table 1 shows the corresponding mean and median statistics. Remarkably GPSRO are closer to the radiosondes above 40 hPa in both mean and median than the analysis. This is particularly impressive because of the different fingerprints of radiosondes and GPSRO, because of the time coincidence of radiosonde and analysis times, and because the analysis assimilates the radiosonde data at these heights, while GPSRO is independent of the radiosonde data. The table suggests that GPSRO have lower biases than the analysis. Standard and absolute deviations are larger, in part because GPSRO captures temperature fluctuations (e.g. gravity waves) which the model parameterizes, thus eliminating sources of horizontal variability. The standard deviation in table 1 also includes the contribution of a few profiles with unphysically large temperature differences. These profiles are not used in the subsequent diagnostics.

Data selection criteria

The impact of ECMWF stratospheric temperature biases on the estimates of air mass conducive to PSCs has been documented before using comparisons to radiosondes [*Knudsen*, 2003, and references therein]. The novelty in our study is that the GPSRO data are independent of the analysis (the radiosondes used for that comparison were assimilated into ECMWF), and the global coverage and the high vertical resolution of GPSRO allow to directly examine the global impact of temperature fluctuations. These fluctuations have been proposed as a dominant cause of conditions leading to Arctic PSCs.

Figure 3.

One would like to eliminate GPSRO profiles that appear at the ends of the histograms in figure 1 bottom. Given the paucity of validation sources in the polar regions, one approach to selecting “valid” GPSRO profiles is to compare against the ECMWF analysis and require that differences remain within a range [*Hajj et al.*, 2002]. A drawback of this approach is the risk of discarding GPSRO profiles

that capture errors in the analysis. Figure 3 illustrates this by showing a consequence of the seasonal behavior described in figure 1 top. Figure 3 shows in black the monthly number of GPSRO profiles where temperatures and refractivities are within 10K and 10% respectively of the interpolated analysis at all heights above 4 km. This is compared to the total weekly number of occultations in grey. The left plot is for the Arctic region. The total number of retrieved profiles follows a variability which can be traced back to operational changes and availability of the data retrieved specifically for this study. For instance, the drop in total number occurred during one week of June 2004, was caused by having to use different types of orbit solutions. We do not include this week to preserve the homogeneity of our dataset and because this week would not affect the conclusions of our current study. Another drop in February 2005 is due to our not using SAC-C occultation profiles after this date. On the other hand, the percentage of profiles meeting the 10K-10% criterion is systematically lower in the winter months, following a cycle independent of the operational changes. The right figure shows that the same occurs in the Antarctic region south of 65°S. There is no reason why occultations should underperform in the local polar winter seasons, and we listed in the previous section some of the problems that the analysis faces. Given the good agreement between GPSRO and radiosondes, we believe that the discrepancies found are more likely to reflect errors in the analysis temperatures.

Figure 4.

We compare in our work results based on requiring three selection criteria that seek profiles with small biases between GPSRO and ECMWF. The first criterion (termed from now on as criterion 1) required GPSRO and the interpolated ECMWF-TOGA to be within 10 K in temperature and within 10% in refractivity of each other at all heights between 11 km and 41 km. Criterion 2 required refractivity differences at the temperature initialization height of 41 km, ε_N, to be under a threshold ($|\varepsilon_N| < 0.05, 0.03$ were used). Note that, from formula (3), if the refractivity difference between analysis and occultation is $\varepsilon_N = 0.1$ at $z_o = 41$ km and $T_e(z_o) \gtrsim 200$ K, the induced retrieval error

can reach $|T_r(z_o) - T_o(z_o)| \gtrsim 20$ K. In criterion 3, the mean absolute deviation over 37 km–41 km had to be below 5 K for each profile (value based on the deviation against radiosondes at 10hPa in table 1), thus eliminating the GPSRO soundings with large sharp temperature structures within their uppermost few km. These criteria, which skew the comparison towards ECMWF-alike profiles, ensure that the analysis biases play a minor role in our comparisons and that differences are mostly due to features substantially smaller than the scale height where anomalies often exceed 1K and can be important contributors to PSC formation [*Carslaw et al.*, 1999; *Dörnbrack et al.*, 1999, 2001, e.g.].

Table 2.

Table 3.

Table 2 shows the number of GPSRO measurements available based on these selection criteria. For illustration, out of 1200 GPSRO profiles captured north of 65°N in December 2001, 220 passed the first criterion, 159 (207) passed the first two when $|\varepsilon_N| \leq 3$ (≤ 5), and only 156 (203) passed the three. We discuss below the impact of these selections on the estimates of air mass conducive to PSCs.

To increase the number of profiles in our statistics beyond the values in rows (a) and (b) of table 2, we compared also to results when the first criterion is applied only to a height range starting at the higher of the lapse rate tropopause or 11 km, and going up to 32 km. The 32 km limit is chosen to include diagnostics at the 10 hPa level, since this level is required to identify stratospheric warmings as defined by the WMO (see next section). Figure 4 shows that the 10 hPa level oscillates between 29 km and 31 km. Temperature errors of 3 K near 40 km have been shown to decay by at least a factor of 4 at 30 km [*Hajj et al.*, 2004, e.g. in figure 8b] where they reach the sub-Kelvin level. This is confirmed in figure 1 which shows that the mean $T_r(z) - T_e(z)$ differences reach their extrema below 2 K at 35-41 km, and 3 K for the 2004/2005 winter. Dividing by a factor of 4 suggests that "true" $T_r(z) - T_o(z)$ temperature errors enter on average sub-Kelvin values at 32 km. Table 3 shows the temperature differences of GPSRO meeting these criteria to coincident radiosondes. It supports our conjecture and shows that GPSRO mean differences outperform the analysis even more than in table 1 and raises the

confidence in GPSRO temperatures in case of disagreements with the analysis.

When the biases between GPSRO and analysis do not impact the study [*Tsuda et al.*, 2000; *Hajj et al.*, 2004; *Wickert et al.*, 2004, e.g.], GPSRO can use more permissive selection criteria. The impact of this will be discussed below. Typically requiring only criterion 1 up to 32 km provides a higher throughput as is illustrated on the two bottom rows of table 2. Inspection of the GPSRO profiles that failed the different criteria in Table 2 showed that a large number of them had large amplitude temperature fluctuations in the height range from 32 km to 41 km. That is why applying criteria 2 and 3 leaves about the same occultation profiles as applying criterion 1 with the conditions (a) or (b). Figure 5 shows two discarded temperature profiles where the criteria described in the next section for PSC temperature thresholds were crossed. These two SAC-C GPSRO profiles captured features sharper and colder than the analysis at similar heights. The soundings are separated by nearly 24 hours and 500 km. Thick solid lines are for the GPSRO and the interpolated ECMWF-TOGA on the 11th of December at latitude 71°N and 16°W. Thin dashed black and grey lines correspond to the nearest occultation on the 12th of December at latitude 68°N and 23°W. One profile is consistent with ice PSCs. The interpolated ECMWF-TOGA (in the thick and dashed grey lines) is close to the running mean of the fluctuating GPSRO profiles. The GPSRO temperature fluctuations increase above 32 km, which enters the range where bending angle noise is known to increase [*Hocke*, 1997]. But this increase in fluctuations is also consistent with a gravity wave whose amplitude increases with height. More work is needed to establish the meaning of these fluctuations above 35 km, and thus we discard this occultation. To discard possible instrumental failure, we confirmed that several GPSRO measured by the same receiver elsewhere just seconds apart from the ones in figures 5 had smooth temperature profiles between 32 km and 41 km. This diagnostic, previous validations of GPSRO waves up to 35 km [*Tsuda et al.*, 2000; *Preusse et al.*, 2000], and the successful comparisons to radiosondes in figure 1 and table 3, suggest

Figure 5.

that the fluctuations are real. These temperature layers are conducive to multi-layered PSCs and ice on December 12. The exclusion criteria conservatively elliminated these and several profiles with temperatures conducive to ice PSCs. However, ice PSCs were observed in this month (see below).

Results

Figure 6.

Figure 6 illustrates the dramatic change in stratospheric temperatures in December of most years. A warming of 35 K is evident at 30 km altitude across the entire Arctic at the end of Dec. 2001. It was preceded by large vertical temperature fluctuations captured by GPSRO.

Figure 7.

Figure 7 shows which of these warmings meet the WMO definition of stratospheric warmings: "a stratospheric warming occurs when the latitudinal gradient in 10-hPa zonal-mean temperatures between 85°N and 60°N is positive for more than 5 days" [*Limpasuvan et al.*, 2004]. Weekly mean temperatures were taken at 10 hPa from the occultation profiles that passed criterion 1 between 32 km and 11 km. The meridional temperature gradient has a complex structure during the transitions from a cold to a warm stratosphere, but the temperature differences between zonal mean temperatures become warmer at the 85° than at the 60° bins during one week, in the last week of December 2001 and 2003. Based on the contours and the colored average values, the pattern looks different in 2003 where there might be a warming in the first and there is one in the fourth week of January, and in 2005 where the second week of February and the first half of March meet the WMO definition. The apparent two year cycle in warmings is consistent with the known influence of the Quasi-Biennial Oscillation (QBO) on the cycle of stratospheric warmings. The QBO was on its east phase during the winters of 2001/02 and 2003/04, while it was on its west phase in 2002/03 [*Labitzke et al.*, 2005].

Figure 8.

Figures 8 show the geographical coverage for all of the GPSRO selection criteria listed in Table 2. The number of profiles increases as the number of selection criteria is lowered. The maps

show that applying criterion 1(a) only many more occultations are left for our study (black plus color symbols) than requiring criteria 1–3(a) (color symbols only). Applying only criterion 1(c) or (d) leaves the densest geographical coverage. Given that the analysis is underperforming in polar winter, disqualifying GPSRO profiles based on the most restrictive criteria 1–3(a) might miss some important geophysical information. As a consequence, we also discuss the global estimates of air mass conducive to PSCs using the most "relaxed" criteria, row (d) on Table 2. Note however, that the error bar of individual profiles of GPSRO stratospheric temperatures increases for such occultations as a result of the possible role of bending angle fluctuations, and the effect of temperature initialization through the analysis which is more likely to introduce the biases described in equation (3).

Figure 9.

Figure 9 shows maps with the locations where PSC temperatures were found in December 2001 under the most stringent and the relaxed criteria. We calculated the temperature thresholds as a function of height for nitric acid trihydrate PSCs (NAT or type I, T$<T_{NAT}$) derived from GPSRO and the interpolated ECMWF-TOGA profiles. NAT PSC formation depends on pressure and chemical composition of the air. Because GPSRO does not measure atmospheric composition, and there are no coincident measurements of the chemical species along the occultation profile, one cannot claim PSC formation, and we focus on temperature thresholds. In figure 9, we used the Hanson-Mauersberger critical temperature for PSC formation [*Hanson and Mauersberger*, 1988] assuming typical stratospheric concentrations of 10 ppbv HNO_3 and a constant H_2O concentration of 5 ppmv H_2O [*Voigt et al.*, 2000; *Müller et al.*, 2001, e.g.]. Under both selection criteria, the profiles were found predominantly between 90°W and 120°E. The profiles that coincide under the "stringent", criterion 1(a), and with the relaxed selection criterion, 1(d), show a robust preference of temperatures conducive to PSCs to occur above land masses. GPSRO however show a denser distribution of PSC profiles than the analysis. We also tested for ice PSC temperatures (type II PSCs, T$<T_{ice}$). Such

temperatures were found near the lapse rate tropopause height (i.e. they are likely to qualify as cirrus) or in occultations with too large temperature fluctuations to pass our selection criteria. As a consequence they are not considered. It is also found that most GPSRO profiles with temperatures conducive to PSCs and where ECMWF-TOGA disagreed (color symbols), are clustered next to profiles where both did find temperatures conducive to PSCs (black symbols) in 9. This increases the probability that most GPSRO profiles with temperatures conducive to PSCs are plausible even under the relaxed selection criterion. The different symbols in figure 9 do not suggest a clear horizontal propagation pattern for PSC formation but rather localized sources of cooling.

Figure 10.

The large number of geographic clusters and coincidences suggests that horizontal mapping of cold air conducive to NAT PSCs derived from GPSRO and ECMWF would yield similar horizontal extents of such cold air masses. This is also found for NAT PSCs in figure 10 which shows a related PSC prediction metric: the daily number of profiles which crossed the temperature threshold for NAT PSCs derived from GPSRO and the interpolated ECMWF-TOGA profiles in December 2001 when only criterion 1 is required. Another PSC temperature criterion, the number of profiles crossing the STS threshold, defined as T_{STS} = T_{NAT} - 3.5 K, is shown in 10 bottom [*Tabazadeh et al.*, 1994; *Carslaw et al.*, 1994]. Both metrics are shown for criterion 1(a) (left column) and criterion 1(d) (right column). The search for STS temperatures finds more frequent disagreement between ECMWF and GPSRO. The figures capture some of the different thresholds for PSC formation found in the literature. We have ignored in our study several factors that can influence the final numbers. First is that HNO_3 and H_2O concentrations change with the distance from the polar vortex boundary and often exceed 10 ppbv, and 5 ppmv [*Lahoz et al.*, 1994] respectively so that higher temperatures might still lead to PSCs [*Müller et al.*, 2001]. A second factor is that wind speed variations with latitude can also influence the total air mass passing through cold regions and exposed to PSC forming temperatures. Such changes in wind

speeds are not accounted for in this study.

A third data source that established the accuracy of the larger GPSRO fluctuations could not be found. However, a possible *lower bound* for the impact of fluctuations on the PSC budget can be set by comparing the histograms of figures 10 to the bottom two rows of 11 where the most stringent selection constraints GPSRO to be very close to the analysis. It is found that the second half of December most STS PSC conditions are absent in ECMWF and found in GPSRO, suggesting that they are associated with waves. Figures 10 and 11, the last of them using all the combinations of selection criteria (a) and (d) in table 2, show that ECMWF-TOGA systematically underestimated the number of profiles with temperatures below T_{NAT} and T_{STS} on December 2001. Similar comparisons to NCEP displayed still larger differences with GPSRO. According to ECMWF-TOGA, temperatures below T_{NAT} occurred only after December 6, while occultations detected adequate temperatures from the first day to the 22nd. The relatively low number of vertical levels included in ECMWF-TOGA is one possible cause for this discrepancy. However, since the full ECMWF analysis uses parameterized representations of gravity waves, it is unlikely to capture specific fluctuations measured by the observations. Another cause might be that the coarse horizontal resolution in the original ECMWF inhibits dynamical processes which produce small scale structures such as mountain waves, whose simulated spectrum strongly depends on the horizontal resolution of the model runs. We discuss next indirect evidence suggesting that PSCs do form when temperatures cross the threshold.

Figure 11.

Figure 12.

Layered PSC structures have been reported before from airborne instruments. Balloon-borne backscatter measurements carried under the Comprehensive Investigation of Polar stratospheric Aerosols (CIPA) out of Esrange, Sweden, in the evening of December 9th, 2001 measured PSCs as high as between 21 and 26.5 km [*Arlander et al.*, 2002; *Kivi et al.*, 2003; *Deshler et al.*, 2003]. Multiple layers of PSCs were also observed on December 10 between 21 and 26.5 km at Sodankylä (67°N, 27°E)

with three layers composed of NAT, STS, and ice [*Kivi et al.,* 2003]. In figures 12a and b, backscatter measurements near Sodankylä show that on December 10 and 11, between 21 and 26.5 km, when the temperature crossed the threshold, PSCs did in fact appear. The nearest GPSRO to a backscatter sonde, in figure 12 bottom, is consistent with these observations although it has large fluctuations and did not pass our selection criteria. It meets temperature thresholds for ice PSCs and bears similarity to the Sodankylä temperature profiles near 23-26 km. Other occultations showed large fluctuations near this location on the 10th, 11th and 12th, but were not selected for the statistics of figures 10 and 9 although temperature fluctuations of $\sim$22 K peak-to-peak have been observed [*Dörnbrack et al.,* 1999, e.g.].

Seasonal cycle

The choice of water vapor concentration has a measurable impact on the threshold temperatures for PSCs and thus in our analysis. To see if the results in the previous section remain robust when the water vapor seasonal cycle is considered we repeated the same analysis described for December 2001, but for all months where there is GPSRO coverage from CHAMP and SAC-C with a simulated seasonal cycle. Given the absence of coincident water vapor measurements at the occultation locations, we simulated the humidity seasonal cycle by calculating the lowest saturation mixing ratio below 15 km for each GPSRO profile and assumed that it remained constant above that height. Whenever such saturation mixing ratios corresponded to volume fractions exceeding 10 ppmv or below 2 ppmv, we considered it as an unlikely value and took 5ppmv. The choice of these values keeps the average water vapor concentration close to the values reported in *Lahoz et al.* [1994] and *Knudsen* [2003]. The resulting histograms, in figure 13, show that the analysis still underestimates the number of profiles with PSCs in most months. Figure 13 shows the monthly number of profiles with temperatures colder than T_{NAT} and T_{ice} above 5 km for occultation and analysis if a water vapor seasonal cycle is simulated

Figure 13.

at the occultation locations. Superimposed is a measure of temperature fluctuations: the monthly mean absolute deviation of all temperature profiles from the filtered version above the lapse rate tropopause. Several measures of temperature fluctuations are found in the literature [*Steiner and Kirchengast*, 2000; *Tsuda et al.*, 2000] which are influenced by the method used to determine the smooth background temperature used as a reference against the fluctuating profile. Our filter serves to determine the month with largest variability, and was inspired in the cos2 filter from *Steiner and Kirchengast* [2000]. The filtered profile was obtained by doing the FFT of the profile deviation from its least squares fit to a fourth order polynomial. The FFT was multiplied by $[1 - \cos(2\pi f/n)]/(2N)$ and zero beyond the first cycle (if $f/n > 1$), where f is a selected peak frequency, N the area normalization constant, and n is a scale to cut off wavelengths below 8 km. The inverse FFT of this windowing was added to the polynomial fit to provide the smooth profile. Sample smooth profiles are seen in dashed black and grey in figure 12c. This filter will characterize sharp temperature structures, such as sharp lapse rate tropopauses, as a fluctuation. To discard the contribution by the tropopause only temperature deviations from their filtered profile were counted as a fluctuation if they occurred above 11 km and at least 1 km above the lapse rate tropopause. The months with largest number of profiles with temperatures conducive to PSC were months 2 (December 2001), 14 (December 2002), 26 (December 2003), and 38 (January 2005) in figure 13 and coincide with or follow (in 2003) the first winter month with largest fluctuation activity in GPSRO. The month of maximum fluctuation activity in ECMWF also coincided with the largest amount of air mass conducive to PSCs except in 2003, where the maximum fluctuations occurred in October 2003, and in 2005.

Impact of temperature differences on each profile

The histogram in figure 13 shows some discrepancies in the number of GPSRO and ECMWF profiles. In the following we discuss what is the relative importance of these differences in terms of the vertical extent of the air masses conducive to PSCs.

Figure 14.

Under the assumption of hydrostatic balance, the pressure difference between the top and bottom of each air layer crossing the PSC temperature threshold equals the weight of air per unit area within which PSCs can form. If the air masses with T<T_{NAT} during December 2001 were added into an air column of unit area, the total weight per unit area exerted by that column would be 331·10^2 Nm^{-2} for ECMWF-TOGA and 425·10^2 Nm^{-2} for GPSRO under the stringent selection 1–3(a) of Table 2. The total weight per unit area exerted by that column would become 746·10^2 Nm^{-2} for GPSRO under the relaxed selection 1–3(d) of Table 2. 626·10^2 Nm^{-2} for ECMWF-TOGA. Figure 14 shows the monthly columns of air mass below the T_{NAT} threshold for the observations and analysis for a constant water vapor concentration of 5 ppmv. To reduce the contribution by the tropopause, we checked that the analysis was applied only to heights which were at least 1 km above lapse rate tropopause and above 11 km. Superimposed is the height with the coldest temperature in the lower stratosphere. This plot shows which months had the largest potential for PSC formation. As illustrated in figures 6, after a stratospheric warming the coldest point drops down approaching the height of the lapse rate tropopause. It is seen that the months with largest amounts of PSC air coincide with or precede the months with nighttime stratospheric warmings. The relative masses of ECMWF compared to GPSRO is shown in percentage in figure 14 bottom. For the most active months, ECMWF underestimated the mass budget in December of 2001, and 2003, while overestimating it in December 2002 (under the relaxed selection criterion) and in January 2005. The overestimate in the winter of 2002/03 agrees with previously reported results of the comparisons to radiosondes [*Knudsen*, 2003], which again confirms the strong

plausibility of the results with the relaxed selection criteria. To illustrate the impact of the selection criteria on mass budgets, figure 14 includes in the bottom dashed line the relative budgets if criteria 1–3 are used with the limits from 11 km to 32 km. The difference with the stringent criterion result mostly reflects the differences caused by the sharp temperature fluctuations above 32 km. If the selection were based only on requiring 10 K and 10% refractivity differences, the total weights increase even more at the expense of including more contributions due to temperature biases. The top panel in this figure serves to show the climatological importance of the percentages shown in the bottom panel. For instance, the $\sim$ 23% difference in January 2002 bears much less importance on possible PSC formation than the $\sim$ 22% difference in December 2001 in terms of total air mass.

The difference caused by the simulated seasonal cycle is also visible when compared to 13, because when the water vapor is kept at a constant low value, the warmer winter months do not always show air masses conducive to PSCs, unlike in figure 13.

Summary and conclusions

We think that GPSRO is an important observational approach to understand the scenarios under which PSCs form, and the ultimate role of PSCs in the Ozone depletion budget. Small vertical scale temperature structures conducive to PSC formation can be measured by GPS radio occultations and monthly statistics can be compared to ECMWF analyses. GPSRO profiles have a denser coverage for this purpose and reach higher altitudes than radiosondes. Two of the four winters studied, 2001/02 and 2003/04, showed an underestimate of the amount of air conducive to PSCs by ECMWF. Those of 2002/03 and 2004/05 show an overestimate by the analysis. A similar overestimate has been confirmed for 2002/03 with an independent data set [*Knudsen*, 2003]. It is interesting to note that this biannual character coincides with the changes in the phase of the QBO. We have shown that there are strong

reasons to believe that discrepancies between GPSRO and ECMWF might in fact due primarily to natural temperature fluctuations. We have shown that months with maximum air mass conducive to NAT PSCs coincide with those of polar nighttime stratospheric warmings during the winters of 2001-2005. Peaks in mass occurred in three out of 4 winters during December and early January (e.g. escaping the most focused days of the SOLVE II campaign in 2002/2003 which went from Jan 8 through Feb. 6). Because occultations average the temperature along the GPS signal track, 200–300 km horizontally, the detected fluctuations are most likely to be of synoptic scale, and may therefore have significant impact on the overall PSC budget. This large scale is confirmed by the clustering observed in the map of locations with PSC-prone profiles. The differences between the analysis and GPSRO suggest the possibility of concluding different cold air masses, different types of PSC composition, and the possibility or not of having STS type PSCs. All three differences are relevant to understanding PSC formation.

The conclusions presented here have mostly a robust qualitative character. More detailed and dedicated studies gathering additional data are needed to properly quantify the PSC conditions found each winter. An important factor to consider is the combination of the fluctuation lifetime and the wind velocities: while less than one hour may suffice to trigger PSC formation by mountain wave activity [*Dörnbrack et al.*, 2001], longer periods may be necessary. Additional information on the persistence of the key temperature structures may be needed to causally connect temperature to PSC formation. Our observations e.g. figure 5, indicate that some wave structures may have persisted for several hours.

References

Ao, C. O., G. A. Hajj, B. A. Iijima, A. J. Mannucci, T. M. Schrøder, M. de la Torre Juárez, and S. S. Leroy, Sensitivity of stratospheric retrievals from radio occultations on upper boundary conditions, in *Occultation for Probing Atmosphere and Climate 2*, edited by G. Kirchengast, U. Foelsche, and A. Steiner, vol. to appear, Springer, 2005.

Arlander, W., et al., The northern hemisphere stratosphere in the 2001/02 winter., *Tech. rep.*, Short report by the European Ozone Research Coordinating Unit, Available at http://www.ozone-sec.ch.cam.ac.uk/EORCU/Reports/wr0102.pdf, 2002.

Bevis, M., S. Businger, S. Chiswell, T. A. Herring, R. A. Anthes, C. Rocken, and R. H. Ware, GPS meteorology: Mapping zenith wet delays onto precipitable water, *J. of Appl. Meteor.*, *33*, 379–386, 1994.

Carslaw, K. S., B. P. Luo, S. L. Clegg, T. Peter, P. Brimblecombe, and P. J. Crutzen, Stratospheric aerosol growth and HNO_3 gas phase depletion from coupled HNO_3 and water uptake by liquid particles, *Geophys. Res. Lett.*, *21*, 2479–2482, 1994.

Carslaw, K. S., T. Peter, J. Bacmeister, and S. D. Eckermann, Widespread solid particle formation by mountain waves in the arctic stratosphere, *J. of Geophys. Res.*, *104*, 1827–1836, 1999.

de la Torre, A., T. Tsuda, G. A. Hajj, and J. Wickert, A global distribution of the stratospheric gravity wave activity from GPS occultation profiles with SAC-C and CHAMP, *J. Meteor. Soc. Japan*, *82*, 407–417, 2004.

de la Torre Juárez, M., A case study of the 2001/2002 winter polar arctic stratosphere as inferred from GPS radio occultations, in *Abstracts of the 12th. conference of the Middle Atmosphere*, American Meteorological Society, San Antonio, TX, 2002.

de la Torre Juárez, M., G. A. Hajj, E. R. Kursinski, A. J. Mannucci, and L. J. Romans, Single frequency processing of atmospheric radio occultations., *Int. J. of Remote Sensing*, *25*, 3731–3744, 2004.

Deshler, T., et al., Large nitric acid particles at the top of an arctic stratospheric cloud, *Journal of Geophysical Research*, *108*, 2003, doi:10.1029/2003JD003479.

Dörnbrack, A., M. Leutbecher, R. Kivy, and E. Kyrö, Mountain wave induced record low stratospheric temperatures above northern scandinavia, *Tellus-A*, *51*, 951–963, 1999.

Dörnbrack, A., M. Leutbecher, J. Reichardt, A. Behrendt, K.-P. Müller, and G. Baumgarten, Relevance of mountain wave cooling for the formation of polar stratospheric clouds over scandinavia: Mesoscale dynamics and observations from january 1997, *J. of Geophys. Res.*, *106*, 1569–1581, 2001.

Drdla, K., and E. V. Browell, Microphysical modeling of the 19992000 arctic winter: 3. impact of homogeneous freezing on polar stratospheric clouds, *J. Geophys. Res.*, *109*, 2004, doi:10.1029/2003JD004352.

DSS-UCAR, http://dss.ucar.edu, 2004, we used the ds111.2 data set from NCAR's Data Support Section.

Fjeldbo, F., and V. Eshleman, The bistatic radar-occultation method for the study of planetary atmospheres, *J. of Geophys. Res.*, *70*, 3217–3225, 1965.

Gobiet, A., and G. Kirchengast, Advancements of GNSS radio occultation retrieval in the upper stratosphere for optimal climate monitoring utility, *J. Geophys. Res.*, *109*, doi:10.1029/2004JD005,117, 2004.

Gobiet, A., U. Foelsche, A. Steiner, M. Borsche, G. Kirchengast, and J. Wickert, Climatological validation of stratospheric temperatures in ECMWF operational analyses with champ radio occultation data, *Geophys. Res. Lett*, *32*, doi:10.1029/2005GL022,617, 2005.

Hajj, G. A., E. R. Kursinski, L. J. Romans, W. I. Bertiger, and S. S. Leroy, A technical description of atmospheric sounding by GPS occultation, *J. of Atmos. and Solar-Terr. Phys.*, *64*, 451–469, 2002.

Hajj, G. A., et al., CHAMP and SAC-C, atmospheric occultation results and intercomparisons., *J. of Geophys. Res.*, *109*, Art. no D06,210, 2004.

Hanson, D., and K. Mauersberger, Laboratory studies of the nitric-acid trihydrate - implications for the south polar stratosphere,, *Geophys. Res. Lett.*, *15*, 855–858, 1988.

Hocke, K., Inversion of GPS meteorology data, *Annales Geophysicae*, *15*, 443–450, 1997.

Kivi, R., E.Kyrö, A.Dörnbrack, and T.Birner, Polar stratospheric cloud observations in northern finland during the recent winters, in *Proc. Sixth European Symposium on Stratospheric Ozone*, edited by N. Harris, G. Amanatidis, and J. G. Levine, Commission of the European Communities, Brussels, p. 245-249, 2003, Göteborg.

Knudsen, B., On the accuracy of analysed low temperatures in the stratosphere, *Atm. Chem. and Phys.*, *3*, 1759–1768, 2003.

Kursinski, E. R., G. A. Hajj, J. T. Schofield, R. P. Linfield, and K. R. Hardy, Observing earth's atmosphere with radio occultation measurements using the global positioning system, *J. Geophys. Res.*, *102*, 23,429–23,465, 1997.

Kursinski, E. R., G. A. Hajj, S. S. Leroy, and B. Herman, The GPS occultation technique, *Terrestrial Atmospheric and Oceanic Sciences*, *11*, 53–114, 2000.

Kursinski, E. R., et al., Initial results of radio occultation observations of earth's atmosphere using the global positioning system, *Science*, *271*, 1107–1110, 1996.

Labitzke, K., B. Naujokat, and M. Kunze, The lower arctic stratosphere in winter since 1952: an update, *SPARC Newsletter 24*, World Clim. Res. Programme, Toronto, 2005.

Lahoz, W. A., et al., Three-dimensional evolution of water vapour distributions in the northern hemisphere as observed by mls, *J. of the Atmos. Sci.*, *51*, 2914–2930, 1994.

Larsen, N., et al., Formation of solid particles in synoptic-scale arctic pscs in early winter 2002/2003, *Atm. Chem. and Phys.*, *4*, 2001–2013, 2004.

Limpasuvan, V., D. W. Thompson, and D. L. Hartmann, The life cycle of the northern hemisphere sudden stratospheric warmings, *J. of Climate*, *17*, 2584–2596, 2004.

Manney, G. L., J. L. Sabutis, S. Pawson, M. L. Santee, B. Naujokat, R. Swinbank, M. E. Gelman, and W. Ebisuzaki, Lower stratospheric temperature differences between meteorological analyses in two cold arctic winters and their impact on polar processing studies, *J. Geophys. Res.*, *108*, 8328,doi:10.1029/2001JD001,149, 2003.

Montzka, S. A., et al., Scientific assessment of ozone depletion: 2002, *Global Ozone Research and Monitoring Project - Report No. 47 Report No. 47*, WMO (World Meteorological Organization), Geneva, 2003.

Müller, M., R. Neuber, G. Beyerle, E. Kyrö, R. Kivi, and L. Wöste, Non-uniform psc occurrence within the arctic polar vortex, *Geophys. Res. Lett.*, *28*, 4175–4178", 2001.

Preusse, P., S. D. Eckermann, and D. Offermann, Comparison of global distributions of zonal-mean gravity wave variance inferred from different satellite instruments., *Geophys. Res. Lett.*, *27*, 3877–3880, 2000.

Randel, W. J., and F. Wu, Cooling of the arctic and antarctic polar stratospheres due to ozone depletion, *J. of Climate*, *12*, 1467–1479, 1999.

Rex, M., R. J. Salawitch, P. von der Gathen, N. R. P. Harris, M. P. Chipperfield, and B. Naujokat, Arctic ozone loss and climate change, *Geophys. Res. Lett.*, *31*, L04,116,doi:10.1029/2003GL018,844, 2004.

Rocken, C., et al., Analysis and validation of GPS/MET data in the neutral atmosphere, *J. of Geophys. Res.*, *102*, 29,849–29,866, 1997.

Schrøder, T. M., C. O. Ao, and M. de la Torre Juárez, Sensitivity of GPS occultation retrieval to the stratopause, *J. of Geophys. Res.*, 2005, submitted.

Steiner, A., and G. Kirchengast, Gravity wave spectra from GPS/MET occultation observations, *Journal of Atmospheric and Oceanic Technology*, *17*, 495–503, 2000.

Tabazadeh, A., R. P. Turco, K. Drdla, M. Z. Jacobson, and O. B. Toon, A study of type i polar stratospheric cloud formation, *Geophys. Res. Letters*, *21*, 1619–1622, 1994.

Thayer, G. D., An improved ecuation for the radio refractive index of air, *Radio Science*, *9*, 803–807, 1974.

Tsuda, T., M.Nishida, C.Rocken, and R.H.Ware, A global morphology of gravity wave activity in the stratosphere revealed by the GPS occultation data (GPS/MET), *Journal of Geophysical Research*, *105*, 7257–7273, 2000.

Voigt, C., A. Tsias, A. Dörnbrack, S. Meilinger, B. Luo, J. Schreiner, N. Larsen, K. Mauersberger, and T. Peter, Non-equilibrium compositions of liquid polar stratospheric clouds in gravity waves, *Geophys. Res. Lett.*, *27*, 3873–3876, 2000.

Wickert, J., T. Schmidt, G. Beyerle, R. König, C. Reigber, and N. Jakowski, The radio occultation experiment aboard champ: Operational data analysis and validation of vertical atmospheric profiles, *Journal of the Meteorological Society of Japan*, *82*, *82*, 381–395, 2004.

Jet Propulsion Laboratory/California Institute of Technology
4800 Oak Grove Dr., Pasadena, CA 91109-8099, U.S.A.

Received June 14, 2005

Submitted to JGR, June 10th, 2005

This manuscript was prepared with AGU's LaTeX macros v5, with the extension package 'AGU^{++}' by P. W. Daly, version 1.6b from 1999/08/19.

Acknowledgments. Fruitful conversations with S.S. Leroy, Y.L. Yung, C.M. Roehl, R. Salawitch, and I. Harris are gratefully acknowledged. Discussions with M. Fromm about POAM III observations for December 2001 provided are gratefully acknowledged. Funding for this work has been provided by NASA through the GEO and GENESIS projects. The research described in this paper was carried out at the Jet Propulsion Laboratory/California Institute of Technology, under a contract with the National Aeronautics and Space Administration.

Figure Captions

Figure 1. Top) Biweekly averaged GPSRO temperature minus ECMWF interpolated to the location and heights of the GPSRO profiles over the whole region north of 65°N. Thin contours around each color are each a half degree, thick contours are each a degree and their value is annotated. **Bottom)** Histogram of differences, radiosondes minus coincident GPSRO. 936 coincidences at 50 hPa and 496 at 10 hPa. Differences larger than 10 K were counted as 10 K. Radiosondes were extrapolated to the GPSRO location using ERA-40 temperature gradients at each height.

Figure 2. Left) Histogram of radiosondes minus coincident GPSRO temperatures. No interpolation in time or space was made to the occultation location. Differences larger than 10 K were counted as 10 K. **Right)** Histogram of radiosondes minus ECMWF temperatures interpolated to the GPSRO location. The analysis times coincided with the radiosondes. Differences larger than 10 K were counted as 10 K.

Figure 3. Left) Total number of weekly occultations north of 65° (in grey), and percentage of occultations (monthly averaged) within 10 K and 10% refractivity agreement with the model at all heights between 41 km and 4 km (in black). **Right)** Same south of 65°.

Figure 4. Biweekly averaged heights of the 10 hPa level over the whole region north of 65°N. Colors and thin contours are each half km. Contours are thicker and annotated at each km mark.

Figure 5. Occultation temperature profile with sharp temperature fluctuations that crossed below T_{NAT} and T_{ice} (thick solid black line). Nearby occultation 1 day later in thin dashed line. The interpolated ECMWF-TOGA is shown for both days in thick solid grey, and thin dashed grey lines. Thin black lines show the thresholds for NAT PSCs T_{NAT} in an atmosphere with 5 ppmv H_20 and 10 ppbv HNO_3, and the colder T_{ice} for ice PSCs.

Figure 6. From top left to bottom right: Five-day averaged GPSRO temperature profiles showing the major warmings for December 2001 to 2003, and for March of 2005, over the whole region north of 65°N.

Figure 7. GPSRO weekly averaged temperature at 10 hPa between November 15 and March 15 for the winters started in 2001, 2002, 2003, and 2004. Averages are weekly into latitude bins of 2.5 degree. Temperatures were interpolated logarithmically to the heights of the 10 hPa level. Colors show the mean value within each 2.5 degree latitude-one week bin starting at a grid line. Red is warmest, blue is coldest. Contours are made using a near-neighbor average search centered around each grid node and labeled each 10 K.

Figure 8. Locations of the occultations studied. Different symbols for each five-day group. Black shows the locations where only criterion 1 (temperature differences less than 10 K and refractivity differences below 10%) is required, color shows the profiles remaining after all criteria 1–3 of Table 2 are applied. **Top left to bottom right:** Limits (a), (b), (c), (d).

Figure 9. Latitudes and longitudes where the Hanson-Mauersberger criterion was met by GPSRO (color) in December 2001. Large open symbols if the criterion was met only by ECMWF. Black symbols add locations where both, the interpolated ECMWF-TOGA and GPSRO, met the criterion. Color legends on top distinguish days with some profiles where only one of the two data sets found temperatures conducive to PSCs. **Left:** Using selection criterion 1 only for the limits in row (a) of Table 2 (i.e. differences below 10 K in temperature 10% in N between 11 km and 41 km). **Right:** Using the same selection criterion for the limits in row (d) (i.e. differences below 10 K in temperature 10% in N between 11 km and 32 km).

Figure 10. Number of daily profiles with temperatures conducive to PSC formation in December 2001 under criterion 1. Grey for GPSRO; black for the interpolated ECMWF-TOGA. **Left column:** for the limits in row (a) of Table 2 (i.e. differences below 10 K in temperature 10% in N between 11 km and 41 km); **right column:** for the limits in row (d) of Table 2 (i.e. differences below 10 K in temperature 10% in N between 11 km and 32 km). Rows are described from top to bottom. **Top row:** Under the Hanson-Mauersberger threshold for NAT PSCs at 5 ppmv water vapor and 10 ppbv HNO_3; **bottom row:** Black line with circles for the number of GPSRO profiles with temperatures conducive to STS.

Figure 11. Same as in figure 10 but adding selection criteria 2 and 3 on rows (a) and (d) of Table 2. Grey for GPSRO; black for the interpolated ECMWF-TOGA.

Left column: for row (a) in Table 2; **right column:** for row (d) in Table 2.

Rows are described from top to bottom.

Upper two rows: Hanson-Mauersberger and STS thresholds for PSCs when selection criterion 2 is added to the criterion 1 in figure 10; **bottom two rows:** The same when selection criterion 3 is added to criteria 1 and 2.

Figure 12. Balloon borne aerosol backscatter sonde measurements near Sodankylä **a) and b) Left columns:** top on Dec. 10 near 14:21 hrs. and bottom 11 near 18:30 hrs. Thick line: the measured backscatter at 940 nm; thin line for 490 nm. **Right columns**: Corresponding temperature profiles. Threshold temperatures $T_{ice} < T_{STS} < T_{NAT}$ appear as straight solid lines. The sondes measure aerosol backscatter at wavelengths $\lambda = 490$ and 940 nm with an average vertical resolution of 30 m. The backscatter ratio R_λ is defined as the ratio of total (i. e. aerosol and molecular) to molecular backscatter. Pressure, temperature, ozone density, and tropospheric relative humidity are measured simultaneously. The instrument signal noise relevant for the measurements is of the order of 1%. **Bottom** GPSRO (black) and interpolated ECMWF-TOGA (grey): **c)** Occultation on Dec. 11th at 16:01, 67.2°N, 11°E, 658 km apart from Sodankylä, showing temperatures conducive to ice. Dashed lines show FFT-smoothed profiles for GPSRO and ECMWF. Threshold temperatures $T_{ice} < T_{STS}\ T_{NAT}$ appear as straight solid lines.

Figure 13. Monthly percentage of profiles (over the total number of soundings) with some air at T<T_{NAT} between Nov 2001 and June 2005 (thick black lines) after applying selection criteria 1–3(d). For these histograms a water vapor seasonal cycle has been simulated. T' is the monthly mean absolute deviation from the smoothed profile temperatures (thin black for GPSRO, ECMWF in thin grey). Blue shows the percentage of profiles with type II PSCs from GPSRO. Red for the ECMWF.

Figure 14. Top) Total weight per unit area of the monthly column of air with T<T_{NAT} above 11 km and north of 65° N (GPSRO in black and grey dashed; ECMWF-TOGA in circles). Height of stratospheric temperature minimum (red open circles). **Bottom)** Relative monthly mass of air columns with T<T_{NAT} for ECMWF-TOGA, in percentage of GPSRO mass, for the stringent 1–3(a) (black) and the relaxed criterion 1–3(d) (grey dashed). The horizontal line represents the GPSRO (100%).

Tables

	Radiosonde–GPSRO and Radiosonde–ECMWF [K]				
hPa	Mean	Std dev	Median	Mean abs. dev.	N
10	0.76 1.21	7.99 2.21	0.84 1.13	4.48 1.89	667
20	0.49 0.63	8.84 1.95	0.38 0.53	3.18 1.68	920
30	-0.05 0.60	18.59 1.73	0.09 0.54	2.54 1.54	1135
40	0.32 0.22	5.10 1.64	0.05 0.14	2.14 1.44	1175
50	0.31 0.14	4.78 1.74	0.01 0.12	1.96 1.41	1184

Table 1. Statistical moments of the differences from radiosondes for GPSRO and analysis shown in figure 2.

Upper limits	Criterion 1	Criterion 2	Criterion 3
(a) 41 km & $\lvert\varepsilon_N\rvert \leq 3$	220	159	156
(b) 41 km & $\lvert\varepsilon_N\rvert \leq 5$	220	207	203
(c) 32 km & $\lvert\varepsilon_N\rvert \leq 3$	759	325	202
(d) 32 km & $\lvert\varepsilon_N\rvert \leq 5$	759	491	280

Table 2. Number of occultations passing different selection criteria in December 2001. The number reflects how many of the initial 1200 passed each subsequent selection criterion (when applied from left to right).

	Radiosonde–GPSRO and Radiosonde–ECMWF [K]				
hPa	Mean	Std dev	Median	Mean abs. dev.	N
10	0.5151.108	3.96 2.24	0.752 1.082	3.85 1.81	371
20	0.0820.496	2.87 1.93	0.166 0.418	2.52 1.60	535
30	0.001 0.490	2.43 1.75	0.053 0.439	2.34 1.57	674
40	-0.052 0.121	2.051.63	-0.057 0.075	1.95 1.47	699
50	-0.096 0.005	2.19 1.82	0.003 0.013	1.73 1.39	705

Table 3. Statistical moments of the differences from radiosondes to GPSRO and analysis when the analysis and the occultation are within 10K and 10% refractivity differences from each other at all heights between 11 km and 32 km.

Figures

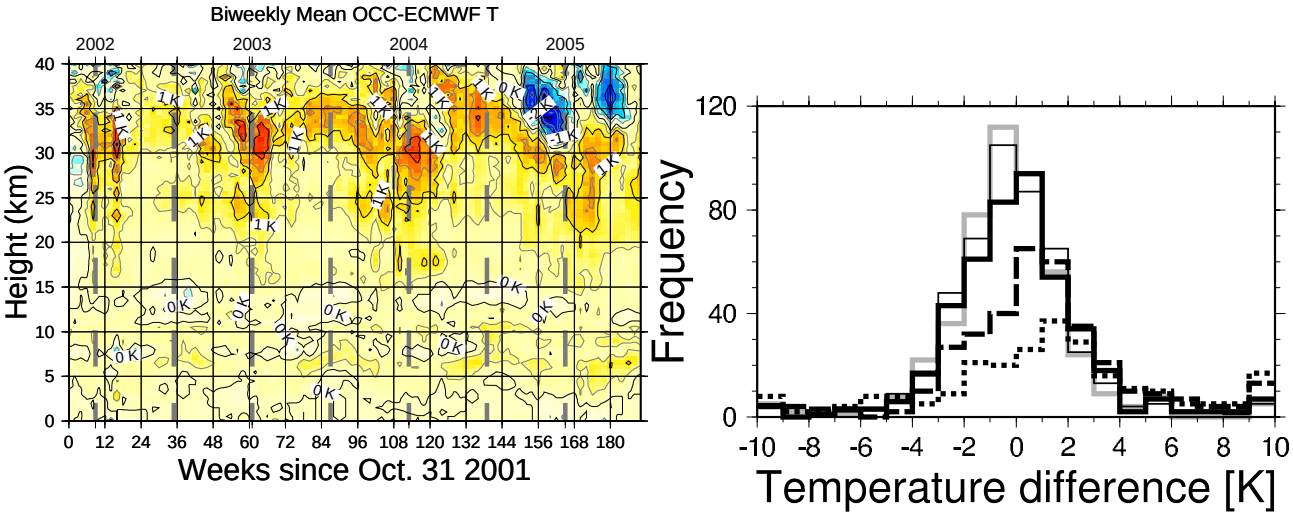

Figure 1. Top) Biweekly averaged GPSRO temperature minus ECMWF interpolated to the location and heights of the GPSRO profiles over the whole region north of 65°N. Thin contours around each color are each a half degree, thick contours are each a degree and their value is annotated. **Bottom)** Histogram of differences, radiosondes minus coincident GPSRO. 936 coincidences at 50 hPa and 496 at 10 hPa. Differences larger than 10 K were counted as 10 K. Radiosondes were extrapolated to the GPSRO location using ERA-40 temperature gradients at each height.

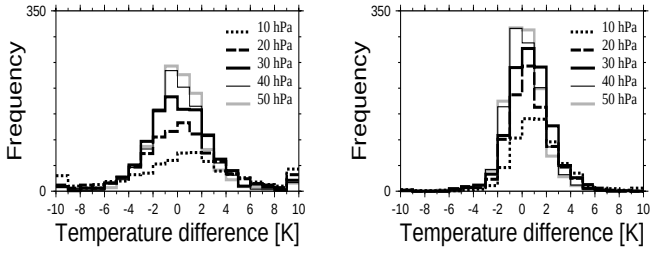

Figure 2. Left) Histogram of radiosondes minus coincident GPSRO temperatures. No interpolation in time or space was made to the occultation location. Differences larger than 10 K were counted as 10 K. **Right)** Histogram of radiosondes minus ECMWF temperatures interpolated to the GPSRO location. The analysis times coincided with the radiosondes. Differences larger than 10 K were counted as 10 K.

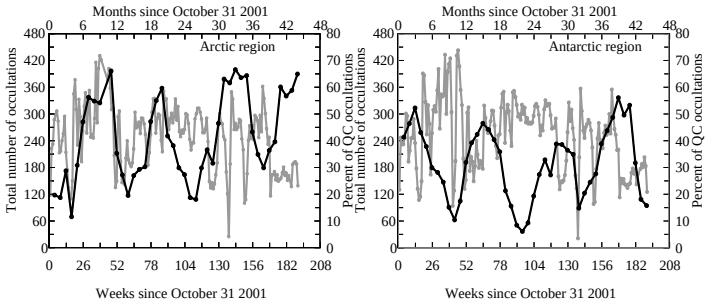

Figure 3. Left) Total number of weekly occultations north of 65° (in grey), and percentage of occultations (monthly averaged) within 10 K and 10% refractivity agreement with the model at all heights between 41 km and 4 km (in black). **Right)** Same south of 65°.

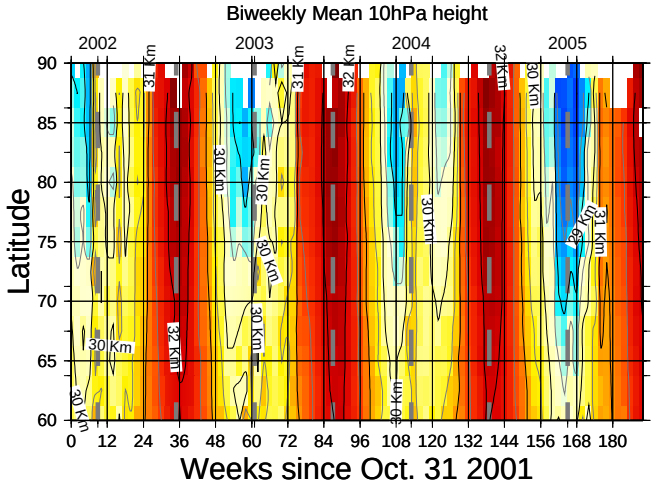

Figure 4. Biweekly averaged heights of the 10 hPa level over the whole region north of 65°N. Colors and thin contours are each half km. Contours are thicker and annotated at each km mark.

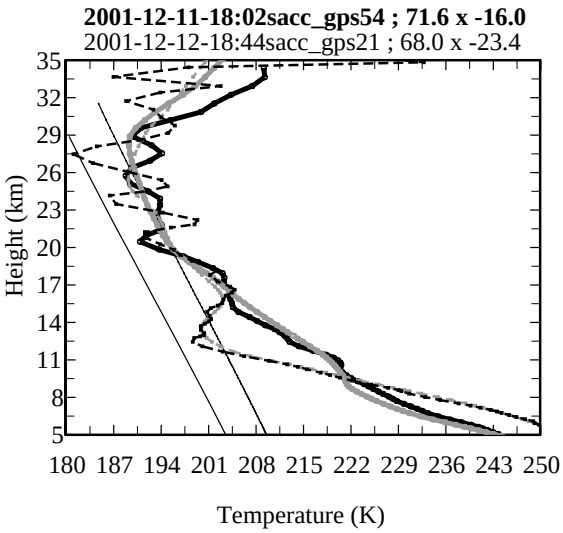

Figure 5. Occultation temperature profile with sharp temperature fluctuations that crossed below T_{NAT} and T_{ice} (thick solid black line). Nearby occultation 1 day later in thin dashed line. The interpolated ECMWF-TOGA is shown for both days in thick solid grey, and thin dashed grey lines. Thin black lines show the thresholds for NAT PSCs T_{NAT} in an atmosphere with 5 ppmv H_20 and 10 ppbv HNO_3, and the colder T_{ice} for ice PSCs.

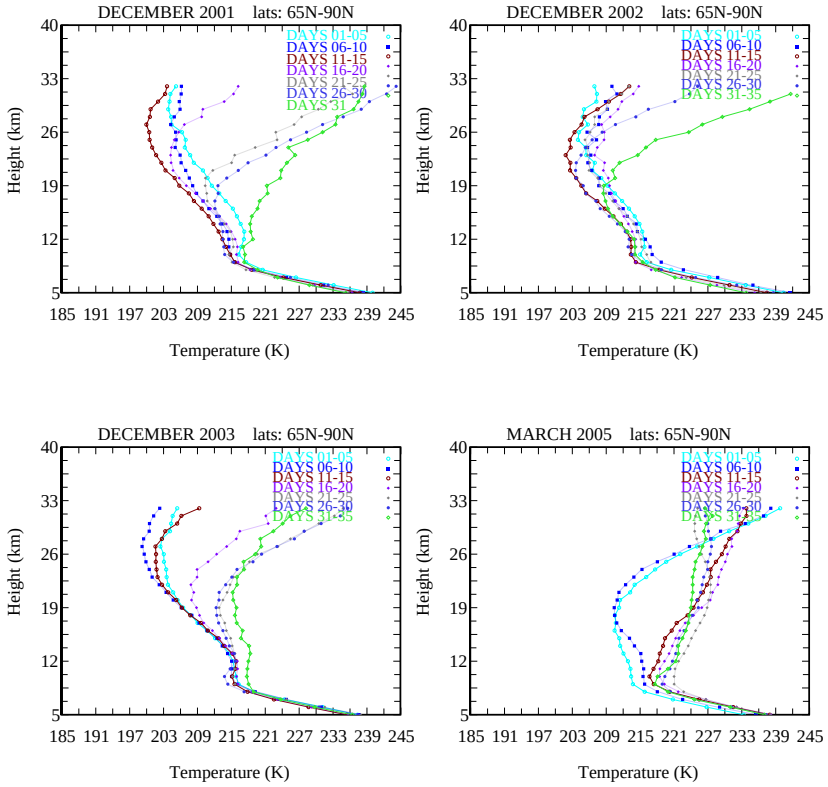

Figure 6. From top left to bottom right: Five-day averaged GPSRO temperature profiles showing the major warmings for December 2001 to 2003, and for March of 2005, over the whole region north of 65°N.

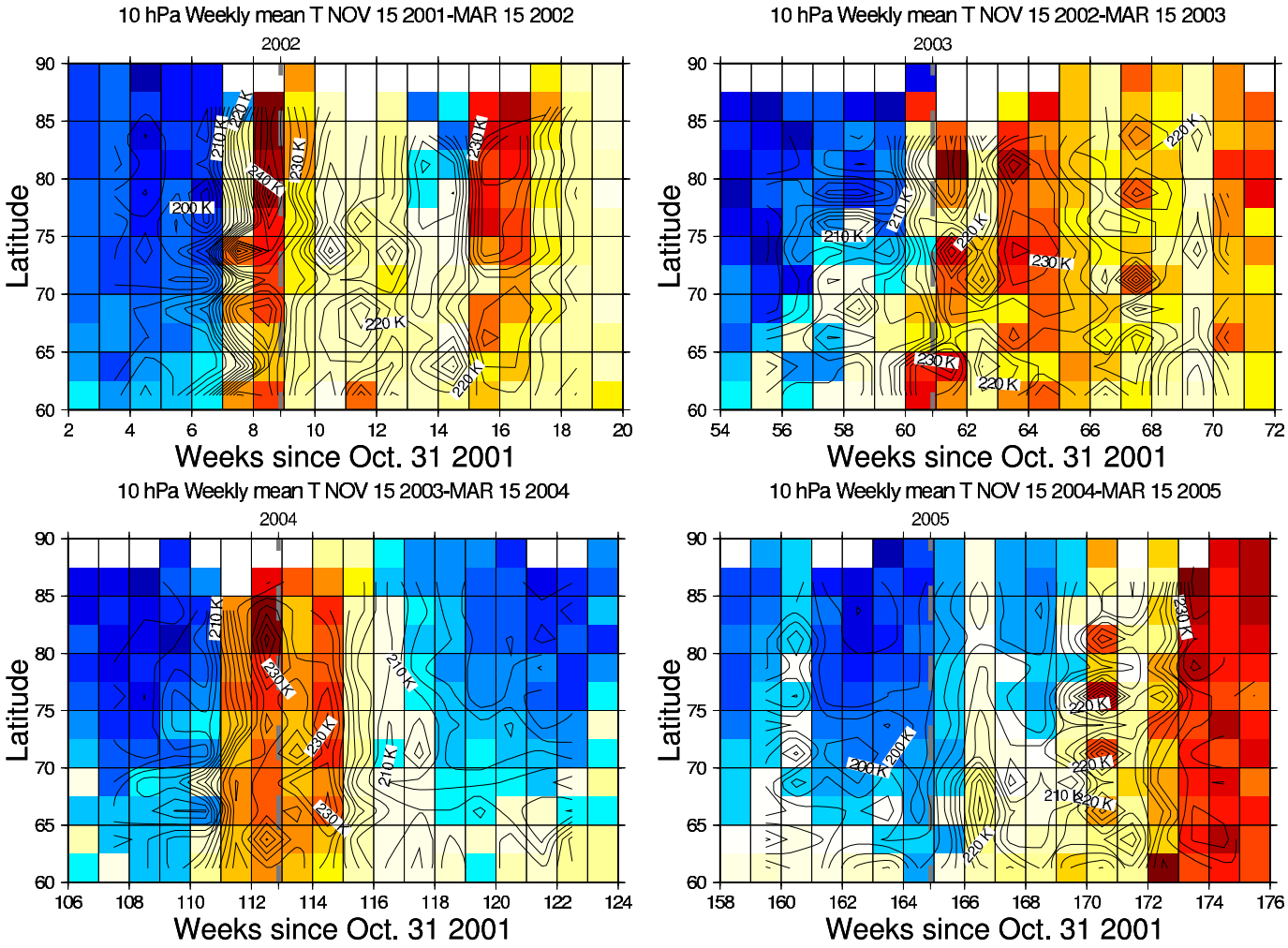

Figure 7. GPSRO weekly averaged temperature at 10 hPa between November 15 and March 15 for the winters started in 2001, 2002, 2003, and 2004. Averages are weekly into latitude bins of 2.5 degree. Temperatures were interpolated logarithmically to the heights of the 10 hPa level. Colors show the mean value within each 2.5 degree latitude-one week bin starting at a grid line. Red is warmest, blue is coldest. Contours are made using a near-neighbor average search centered around each grid node and labeled each 10 K.

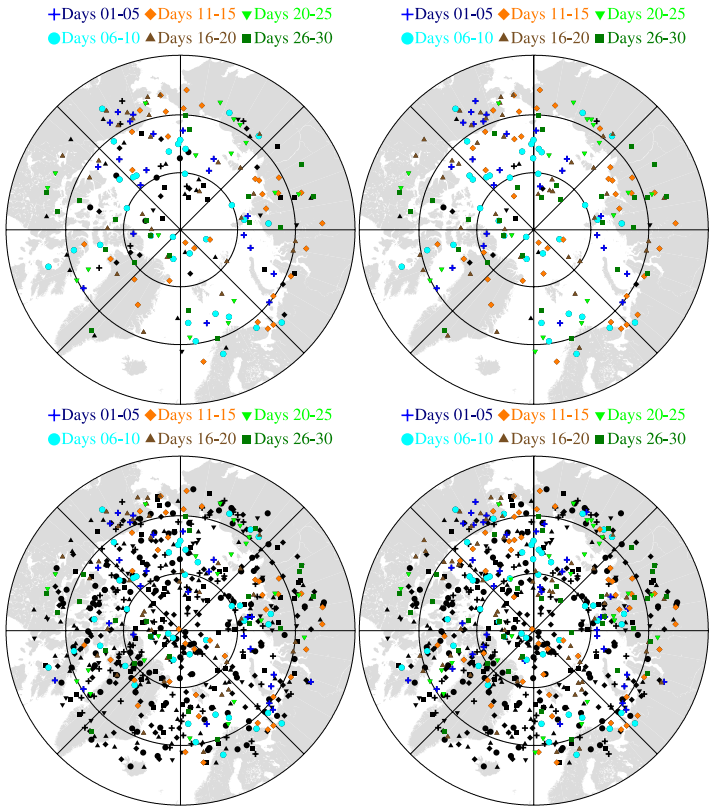

Figure 8. Locations of the occultations studied. Different symbols for each five-day group. Black shows the locations where only criterion 1 (temperature differences less than 10 K and refractivity differences below 10%) is required, color shows the profiles remaining after all criteria 1–3 of Table 2 are applied. **Top left to bottom right:** Limits (a), (b), (c), (d).

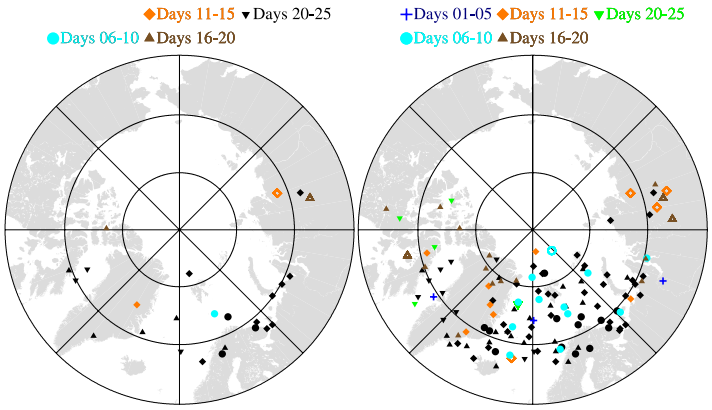

Figure 9. Latitudes and longitudes where the Hanson-Mauersberger criterion was met by GPSRO (color) in December 2001. Large open symbols if the criterion was met only by ECMWF. Black symbols add locations where both, the interpolated ECMWF-TOGA and GPSRO, met the criterion. Color legends on top distinguish days with some profiles where only one of the two data sets found temperatures conducive to PSCs. **Left:** Using selection criterion 1 only for the limits in row (a) of Table 2 (i.e. differences below 10 K in temperature 10% in N between 11 km and 41 km). **Right:** Using the same selection criterion for the limits in row (d) (i.e. differences below 10 K in temperature 10% in N between 11 km and 32 km).

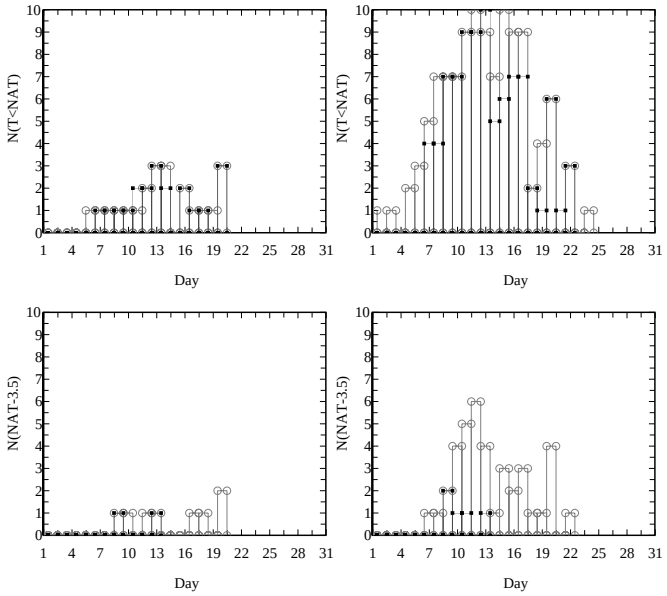

Figure 10. Number of daily profiles with temperatures conducive to PSC formation in December 2001 under criterion 1. Grey for GPSRO; black for the interpolated ECMWF-TOGA.

Left column: for the limits in row (a) of Table 2 (i.e. differences below 10 K in temperature 10% in N between 11 km and 41 km); **right column:** for the limits in row (d) of Table 2 (i.e. differences below 10 K in temperature 10% in N between 11 km and 32 km). Rows are described from top to bottom.

Top row: Under the Hanson-Mauersberger threshold for NAT PSCs at 5 ppmv water vapor and 10 ppbv HNO_3; **bottom row:** Black line with circles for the number of GPSRO profiles with temperatures conducive to STS.

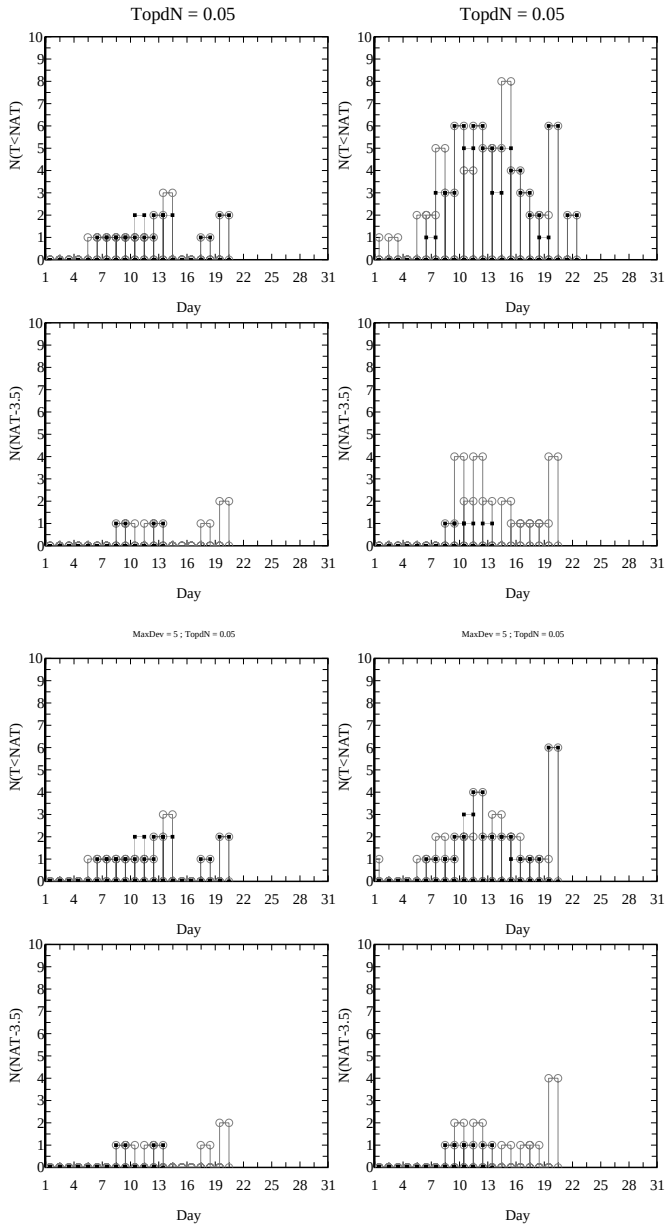

Figure 11. Same as in figure 10 but adding selection criteria 2 and 3 on rows (a) and (d) of Table 2. Grey for GPSRO; black for the interpolated ECMWF-TOGA.

Left column: for row (a) in Table 2; **right column:** for row (d) in Table 2.

Rows are described from top to bottom.

Upper two rows: Hanson-Mauersberger and STS thresholds for PSCs when selection criterion 2 is added to the criterion 1 in figure 10; **bottom two rows:** The same when selection criterion 3 is added to criteria 1 and 2.

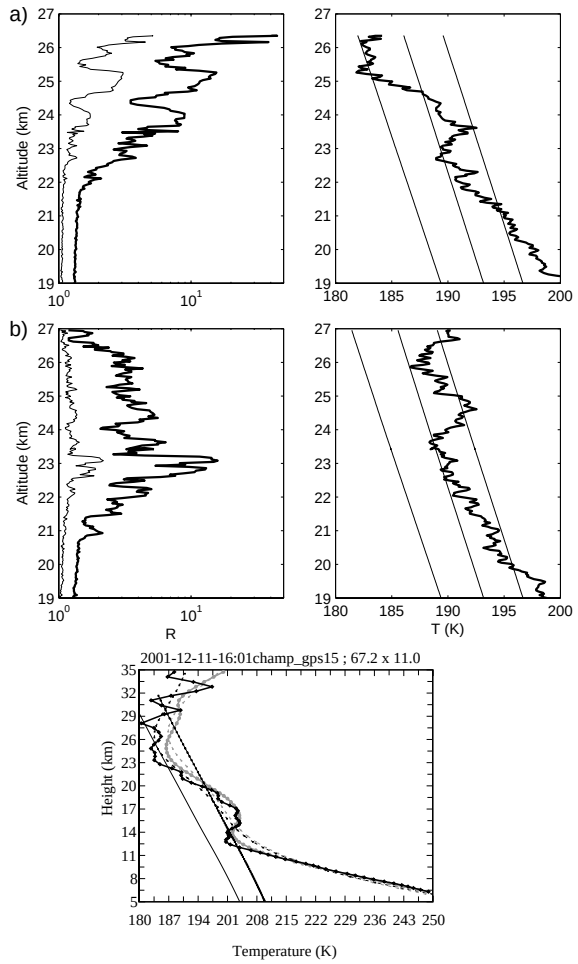

Figure 12. Balloon borne aerosol backscatter sonde measurements near Sodankylä **a) and b) Left columns:** top on Dec. 10 near 14:21 hrs. and bottom 11 near 18:30 hrs. Thick line: the measured backscatter at 940 nm; thin line for 490 nm. **Right columns**: Corresponding temperature profiles. Threshold temperatures $T_{ice} < T_{STS} < T_{NAT}$ appear as straight solid lines. The sondes measure aerosol backscatter at wavelengths $\lambda = 490$ and 940 nm with an average vertical resolution of 30 m. The backscatter ratio R_λ is defined as the ratio of total (i. e. aerosol and molecular) to molecular backscatter. Pressure, temperature, ozone density, and tropospheric relative humidity are measured simultaneously. The instrument signal noise relevant for the measurements is of the order of 1%. **Bottom** GPSRO (black) and interpolated ECMWF-TOGA (grey): **c)** Occultation on Dec. 11th at 16:01, 67.2°N, 11°E, 658 km apart from Sodankylä, showing temperatures conducive to ice. Dashed lines show FFT-smoothed profiles for GPSRO and ECMWF. Threshold temperatures $T_{ice} < T_{STS}\ T_{NAT}$ appear as straight solid lines.

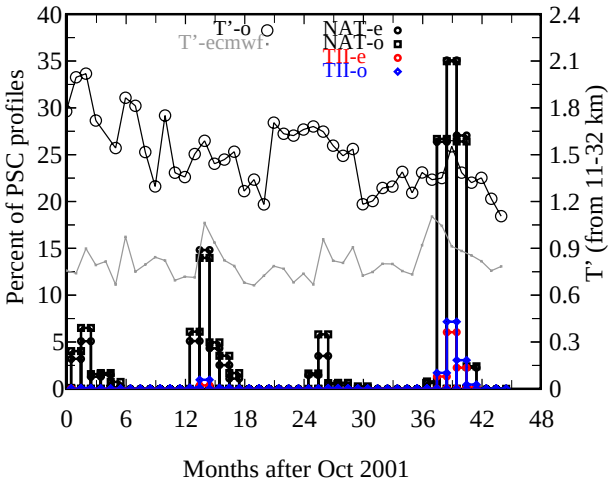

Figure 13. Monthly percentage of profiles (over the total number of soundings) with some air at T<T_{NAT} between Nov 2001 and June 2005 (thick black lines) after applying selection criteria 1–3(d). For these histograms a water vapor seasonal cycle has been simulated. T' is the monthly mean absolute deviation from the smoothed profile temperatures (thin black for GPSRO, ECMWF in thin grey). Blue shows the percentage of profiles with type II PSCs from GPSRO. Red for the ECMWF.

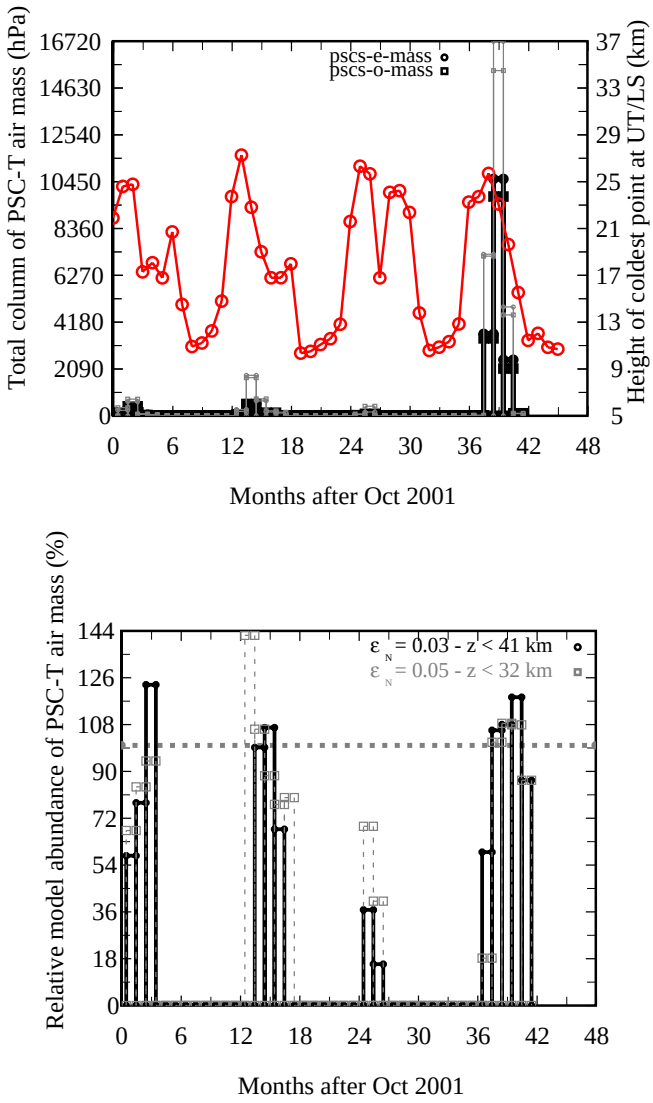

Figure 14. Top) Total weight per unit area of the monthly column of air with T<T_{NAT} above 11 km and north of 65° N (GPSRO in black and grey dashed; ECMWF-TOGA in circles). Height of stratospheric temperature minimum (red open circles). **Bottom)** Relative monthly mass of air columns with T<T_{NAT} for ECMWF-TOGA, in percentage of GPSRO mass, for the stringent 1–3(a) (black) and the relaxed criterion 1–3(d) (grey dashed). The horizontal line represents the GPSRO (100%).